Studies of Atmospheric Noise on Mauna Kea at 143 GHz with Bolocam

J. Sayers[a], S. R. Golwala[a], P. A. R. Ade[b], J. E. Aguirre[c,d], J. J. Bock[e], S. F. Edgington[a], J. Glenn[d], A. Goldin[e], D. Haig[b], A. E. Lange[a], G. T. Laurent[d], P. D. Mauskopf[b], H. T. Nguyen[e], and P. Rossinot[a]

[a] Division of Physics, Mathematics, & Astronomy, California Institute of Technology, Mail Code 59-33, Pasadena, CA 91125 [b] Physics and Astronomy, Cardiff University, 5 The Parade, P. O. Box 913, Cardiff CF24 3YB, Wales, UK [c] Jansky Fellow, National Radio Astronomy Observatory [d] Center for Astrophysics and Space Astronomy & Department of Astrophysical and Planetary Sciences, University of Colorado, 389 UCB, Boulder, CO 80309 [e] Jet Propulsion Laboratory, California Institute of Technology, 4800 Oak Grove Drive, Pasadena, CA 91109

Keywords: atmospheric noise, ground-based instrumentation, water vapor, Bolocam

ABSTRACT

We report measurements of the fluctuations in atmospheric emission (atmospheric noise) above Mauna Kea recorded with Bolocam at 143 GHz. These data were collected in November and December of 2003 with Bolocam mounted on the Caltech Submillimeter Observatory (CSO), and span approximately 40 nights. Below $\simeq 0.5$ Hz, the data time-streams are dominated by the $f^{-\delta}$ atmospheric noise in all observing conditions. We were able to successfully model the atmospheric fluctuations using a Kolmogorov-Taylor turbulence model for a thin wind-driven screen in approximately half of our data. Based on this modeling, we developed several algorithms to remove the atmospheric noise, and the best results were achieved when we described the fluctuations using a low-order polynomial in detector position over the 8 arcminute focal plane. However, even with these algorithms, we were not able to reach photon-background-limited instrument photometer (BLIP) performance at frequencies below $\simeq 0.5$ Hz in any observing conditions. Therefore, we conclude that BLIP performance is not possible from the CSO below $\simeq 0.5$ Hz for broadband 150 GHz receivers with subtraction of a spatial atmospheric template on scales of several arcminutes.

1. INTRODUCTION

A number of wide-field ground-based mm/submm imaging arrays have been commissioned during the past 15 years, including SCUBA,[11] MAMBO,[12] Bolocam,[7] SHARC II,[6] APEX-SZ,[5] LABOCA,[13] ACT,[15] and SPT.[27] Since these cameras are operated at ground-based telescopes, they all see emission from water vapor in the atmosphere. In almost all cases the raw data from these cameras is dominated by atmospheric noise caused by fluctuations in this emission. All of these cameras make use of the fact that the atmospheric water vapor is in the near field, and therefore all of the array pixels record most of the atmospheric noise as a common mode signal that can be removed quite well. The critical issue is the level of common mode rejection that can be achieved and whether this permits recovery of BLIP performance. This paper seeks to quantitatively study the problem using Bolocam data obtained at 143 GHz at the CSO.

As mentioned above, the dominant source of non-removable noise in Bolocam data is fluctuations in emission from the atmosphere. Since water vapor produces most of the emission at millimeter wavelengths, these fluctuations are caused by variations in the column depth of precipitable water between Bolocam and the astronomical

Further author information: (Send correspondence to Jack Sayers)
E-mail: jack@caltech.edu, Telephone: 1 626 395 2892

object of interest*.[4,19,20] Bolocam was designed to have a high degree of overlap between the individual beams as they pass through the atmosphere, so most of the fluctuations in atmospheric emission show up as a common mode signal in all of the bolometers. However, the beams do diverge; the largest separation between beam centers increases by about 2.5 meters per kilometer above the telescope. This divergence is small compared to the $\simeq$ 10 m diameter of the the beams, but the result is that only $\simeq$ 75% of the atmospheric fluctuations can be removed by subtracting the common mode signal. The residual 25% of the atmospheric noise limited the sensitivity of our data, thus motivating further study of these fluctuations. This study focused on two main topics: 1) determining the phenomenology of the atmospheric noise (*i.e.*, can it be modeled in a simple and robust way) and 2) finding more effective ways to remove the atmospheric noise based on this modeling.

1.1 Instrument Description

Bolocam is a large format, millimeter-wave camera designed to be operated at the CSO, and 115 optical detectors were used for the observations described in this paper. Cylindrical waveguides and a metal-mesh filter are used to define the passbands for the detectors, which were centered at 143 GHz with an effective width of 21 GHz.† A cold (4 K) Lyot stop is used to define the illumination of the 10.4 m primary mirror with a diameter of $\simeq$ 8 meters, and the resulting far-field beams have FWHMs of 60 arcseconds. The detector array, which utilizes silicon nitride micromesh (spider-web) bolometers,[21] has a hexagonal geometry with nearby detectors separated by 40 arcseconds, and the field of view is approximately 8 arcminutes. More details of the Bolocam instrument can be found in Glenn et al.,[7] Glenn et al.,[8] Haig et al.,[10] and Golwala et al.[9]

The data we describe in this paper were collected during one 40 night observing run at the CSO in late 2003. During that time we observed two science fields, one centered on the Lynx field at 08h49m12s, +44d50m24s (J2000) and one coinciding with the Subaru/XMM Deep Survey (SXDS or SDS1) centered at 02h18m00s, -5d00m00s (J2000). These are both "blank" fields, which means they contain very little astronomical signal. Therefore, our data are well suited to measure the signal caused by emission from the atmosphere. To map these fields, we raster scanned the telescope at 4 arcminutes/second parallel to the RA or dec axis. Throughout this paper we will refer to single scans and single observations; a scan is one raster across the field and is 12.5 seconds (50 arcminutes) in length and an observation is a set of twenty scans that completely map the science field, which takes $\simeq$ 8 minutes. Our total data set contains approximately 1000 observations, split evenly among Lynx and SDS1. Flux calibration was determined from observations of Uranus and Neptune, and nearby quasars were used for pointing reconstruction. A more detailed description of the data is given in Sayers et al.[28]

1.2 Typical Observing Conditions

Since atmospheric noise from water vapor is generally the limiting factor in the sensitivity of broadband, ground-based, millimeter-wave observations, the premier sites for these observations, which include Mauna Kea, Atacama, and the South Pole, are extremely dry. On Mauna Kea, the CSO continuously monitors the atmospheric opacity with a narrow-band, heterodyne τ-meter that measures the optical depth at 225 GHz (τ_{225}).[3] Since τ_{225} is a monotonically increasing function of the column depth of precipitable water vapor in the atmosphere, these τ_{225} measurements can be used to quantify how dry the atmosphere above Mauna Kea is. Historically, the median value of τ_{225} is 0.091, with the 25% and 75% centiles at τ_{225} = 0.058 and 0.153. For comparison, the median value of τ_{225} at Atacama is 0.061, while the median value at the south pole is around 0.053.[17,25,26,29]

2. KOLMOGOROV-TAYLOR/THIN-SCREEN ATMOSPHERIC MODEL

The Kolmogorov-Taylor model of turbulence provides a good description of air movement in the atmosphere.[14,30,31] According to the model, processes such as convection and wind shear inject energy into the atmosphere on large length scales, of order several kilometers.[14,32] This energy is transferred to smaller scales by eddy currents,

*The column depth of oxygen in the atmosphere also produces a non-negligible amount of emission, a factor of a few less than the emission from water vapor under typical conditions at Mauna Kea. However, the oxygen in the atmosphere is well mixed, and therefore fluctuations in the emission are minimal. In contrast, the temperature of the atmosphere tends to be close to the condensation point of the water vapor, and causes the water vapor to be poorly mixed in the atmosphere. Therefore, there are in general significant fluctuations in the emission from water vapor.[20]

†Bolocam can also be configured to observe at 270 GHz.

until it is dissipated by viscous forces at Kolmogorov microscales, corresponding to the smallest scales in turbulent flow and of order several millimeters for the atmosphere.[14] For a three-dimensional volume, the model predicts a power spectrum for the fluctuations from this turbulence that is proportional to $|\vec{q}|^{-11/3}$, where $\vec{q}$ is a three-dimensional spatial frequency with units of 1/length. The same spectrum holds for particulates that are passively entrained in the atmosphere, such as water vapor.[30]

For our analysis, we adopted the two-dimensional thin-screen model described by Lay and Halverson,[19] and a schematic of this thin-screen model is given in Figure 1 of their paper. This model assumes that the fluctuations in water vapor occur in a turbulent layer at a height $\mathrm{h_{av}}$ with a thickness Δh, where $\mathrm{h_{av}} \gg \Delta\mathrm{h}$. This layer is moved horizontally across the sky by wind at a velocity $\vec{w}$. Given these assumptions, the three-dimensional Kolmogorov-Taylor power spectra reduces to

$$P(\vec{\alpha}) = A\mathrm{h}_{\mathrm{av}}^{5/3} \sin\epsilon^{-8/3} |\vec{\alpha}|^{-11/3}, \tag{1}$$

where A is a measure of the turbulent intensity, ϵ is the elevation angle of the telescope, and $\vec{\alpha}$ is the two-dimensional angular frequency with units of 1/radians.

3. COMPARISON OF DATA TO THEORY

3.1 Instantaneous Correlations

Equation 1 can be converted from a power spectrum in angular frequency space to a correlation function as a function of angular separation. Since the power spectrum is azimuthally symmetric, we can write $P(\vec{\alpha})$ as $P(\alpha)$, where $\alpha = |\vec{\alpha}|$. This power spectrum will produce a correlation function according to

$$C(\theta) = 2\pi \int_0^\infty d\alpha \; \alpha \; P(\alpha) \; J_0(2\pi\alpha\theta), \tag{2}$$

where θ is the angular separation in radians and J_0 is the 0^{th}-order Bessel function of the first kind.[‡] The correlation function produced by the integral in Equation 2 is an infinite series of hyper-geometric functions, which can be reduced to

$$C(\theta) = C_0 + C_1\theta^{\beta-2} + \mathcal{O}(\theta^2) \tag{3}$$

for small values of θ, where $\beta = 11/3$ for the Kolmogorov-Taylor model we have adopted and C_0 and C_1 are functions of several of the physical parameters from the model. Note that C_1 is negative, because the correlation decreases with increasing angular separation. Without loss of generality, Equation 3 can be rewritten as

$$C(\theta) = C_0 + C_1\theta^{\gamma(\theta)}, \tag{4}$$

where $\gamma(\theta) = 5/3$ for $\theta \ll 1$ and $\beta = 11/3$. If atmospheric emission is the only signal in the time-stream, which is a reasonable approximation for Bolocam data, then $C_0 = 1$ and C_1 will be negative. However, Equation 3 is only valid for point-like beams, which is a poor assumption for Bolocam because the beam diameters are $\simeq 10$ m and the separations are of order 1 m. Since the far-field distance for Bolocam is $\simeq 50$ km at 2.1 mm, the beams can be well approximated by a top-hat function with a diameter of 10 m. With this assumption, we can numerically solve for the correlation as a function of angular separation. The result is that $\gamma(\theta)$ varies slightly as a function of separation (*i.e.*, there is some running in the power law), and $1.6 \leq \gamma(\theta) \leq 2.0$ for any physically reasonable height of the turbulent layer over the range of angular separations of the Bolocam beams.

To compare our data to this model, we calculated the relative correlation coefficient between the time-streams of every bolometer pair according to

$$C_{ij} = \frac{\sum_n d_{in} d_{jn}}{\sqrt{\sum_n d_{in}^2}\sqrt{\sum_n d_{jn}^2}},$$

where C_{ij} is the relative correlation between bolometer i and bolometer j, and d_{in} is the time-stream data for bolometer i at time sample n. A single correlation value for each pair was calculated for each 12.5-second-long

[‡]In practice, the integral in Equation 2 diverges as $\alpha \to 0$, so a cutoff is made at α_{min}. This is physically reasonable because there is a maximum length scale for the turbulence.

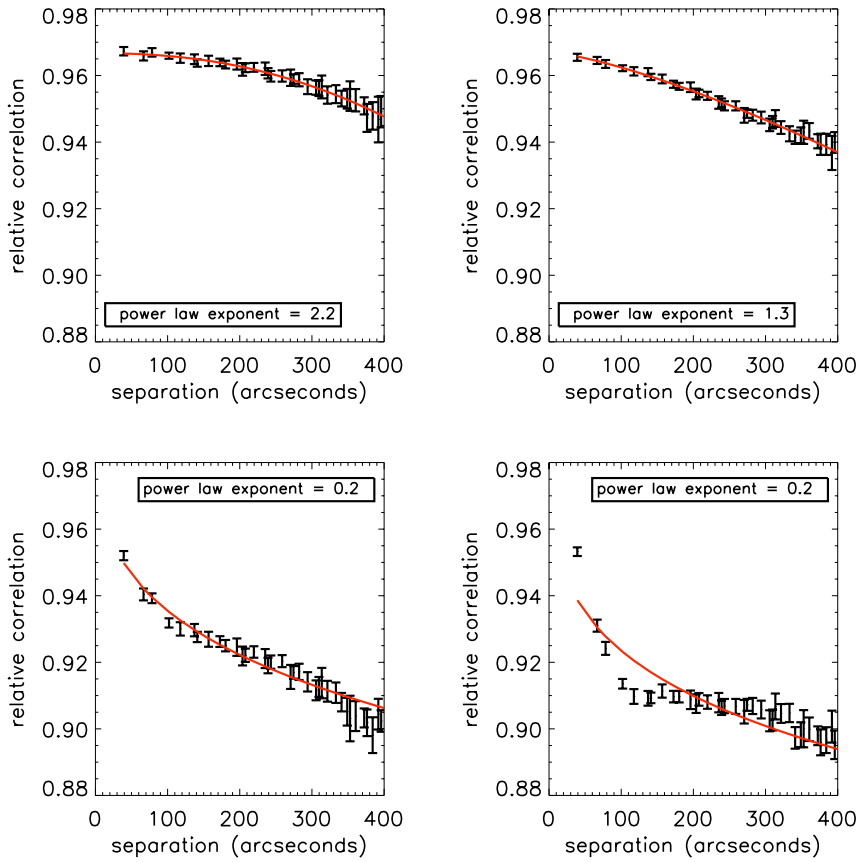

Figure 1. Relative correlation of the time-streams of all bolometer pairs for a single eight-minute-long observation of a science field. Overlaid in red is a fit of the power law given in Equation 5. The power law exponent is expected to be $\sim 1.6 - 2.0$ if the atmosphere is well described by the Kolmogorov-Taylor turbulence model and the thin-screen approximation. The top row shows observations that are relatively well described by the model, and the bottom row shows observations that do not fit the model.

scan made while observing one of the science fields, and then averaged over the twenty scans in one complete observation of the field. Therefore, we have assumed that the atmospheric noise conditions do not change over the eight-minute-long observation. Next, the correlations were binned according to the separation of the bolometer pair and fit to a function of the form

$$C(\theta) = C_0 + e^{a_0 + a_1 \log(\theta) + a_2 \log(\theta)^2}, \tag{5}$$

where C_0, a_0, a_1, and a_2 are free parameters. This functional form was chosen because it is a simple way to represent a running power law. Some examples of the data with a fit overlaid are given in Figure 1. We calculated a fit for all $\simeq 1000$ observations, and 57% of the observations produced a physically reasonable fit with $C_0 \leq 1$. The median power law index for the observations with a valid fit is 1.27, relatively close to the expectation of $1.6 - 2.0$ for a Kolmogorov-Taylor spectrum with $\beta = 11/3$. See Figure 2. In general, we found that observations made in good weather (*i.e.*, less atmospheric noise, characterized by the time-stream RMS) are more likely to produce a good fit to the model than observations made in bad weather.

3.2 Time-Lagged Correlations

Another component in the model described by Lay and Halverson is the wind velocity, $\vec{w}$. If the wind velocity is assumed to be constant, and the spatial structure of the turbulent layer is static on the time scales required

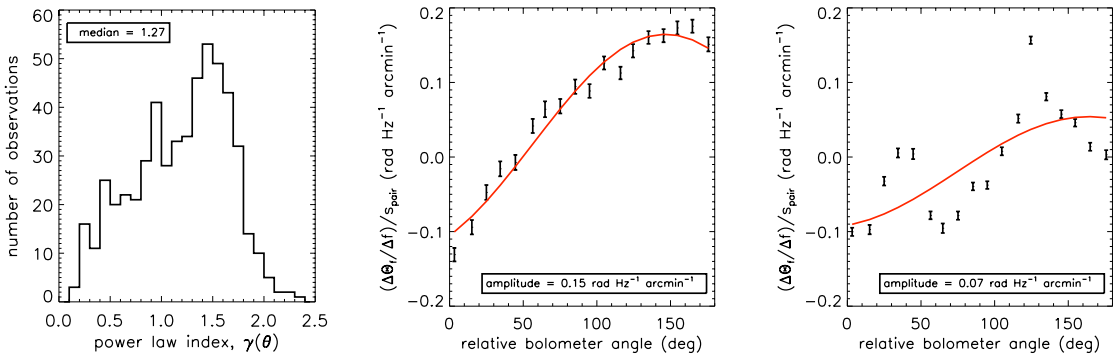

Figure 2. LEFT: Histogram of the average fitted value of $\gamma(\theta)$ from Equation 4 for the 57% of the observations that produced a valid fit of the model. For these fits $\gamma(\theta)$ was assumed to be constant (*i.e.*, no running). Note that $\gamma(\theta)$ is expected to have a value between 1.6 and 2.0 if the Kolmogorov-Taylor exponent $\beta = 11/3$. CENTER and RIGHT: Plots of the slope of Θ_f/s_{pair} versus frequency for all bolometer pairs and all scans of a given observation. This slope is binned according to θ_{pair}, and a sinusoidal fit is overlaid in red. The fit is based only on frequencies where the atmospheric noise is the dominant signal, which is usually $f \lesssim .5$ Hz. The plot on the left comes from an observation taken in relatively good weather and the plot on the right comes from an observation taken in relatively poor weather. In general, the data collected in good weather is well fit by the model, while data collected in bad weather is not.

for the wind to move the layer past our beams,[31] then detectors aligned with the wind velocity will see the same atmospheric emission, but at different times.[4] Making reasonable assumptions for the wind speed (10 m/s) and height of the turbulent layer (1 km) yields an angular speed of approximately 30 arcminutes/sec for the layer. Note that this is much faster than our scan speed of 4 arcminutes/sec. Since the diameter of the Bolocam focal plane is 8 arcminutes, the wind velocity and spatial structures only need to be constant for a fraction of a second to make our assumption valid. To look for these time-lagged correlations, we computed the relative cross power spectrum between every pair of bolometers, described by

$$xPSD_{i,j}(f_m) = \frac{D_i(f_m)^* D_j(f_m)}{\sqrt{|D_i(f_m)|^2}\sqrt{|D_j(f_m)|^2}},$$

where $xPSD_{i,j}(f_m)$ is the relative cross PSD between bolometers i and j, $D_i(f_m)$ is the Fourier transform of the data time-stream for bolometer i at Fourier space sample m, and f_m is the frequency (in Hz) of sample m.

If two bolometers see the same signal at different times, then the cross PSD of these bolometers will have a phase angle described by

$$\tan^{-1}(xPSD) = \Theta_f = 2\pi f \Delta t$$

where f is the frequency in Hz and Δt is the time difference (in sec) between the signal recorded by the two bolometers. Therefore, the slope of a linear fit to Θ_f versus f will be proportional to Δt. If the simple atmospheric model we have assumed is correct, then $\Delta t/s_{pair}$ should be a sinusoidally varying function of the relative angle between the bolometer pair (θ_{pair}), where s_{pair} is the distance between the two bolometers. Analogous to the time-instantaneous model, approximately half of the observations were well fit by this time-lagged model. Some examples of $2\pi\Delta t/s_{pair}$ versus θ_{pair} are given in Figure 2. As with the time-instantaneous model, this model appears to provide a better description of data collected in good weather than data collected in bad weather, and observations that are well described by the time-instantaneous model tend to be well described by the time-lagged model as well.

Using the data that is accurately described by the time-lagged model, we were able to determine the angular speed of the wind. Most of the speeds we inferred were between 10 and 40 arcminutes/second, in good agreement with what we expect for a reasonable wind speed and turbulent height. As an example, the amplitude of the sin wave for the plot on the left of Figure 2 is $0.22 = 2\pi\Delta t$, so $\Delta t = 0.035$ seconds for bolometers that are adjacent (separated by 40 arcseconds). This gives an angular velocity of 20 arcminutes/second, which corresponds to a wind velocity of about 10 km/hr at a height of 500 m, or a wind velocity of about 20 km/hr at a height of 1 km.

3.3 Summary

In summary, the Kolmogorov-Taylor thin-screen model provides an adequate description of approximately half our data. We observe the expected time-instantaneous spatial correlation function and the appropriate time-lagged correlations due to wind. It is not clear why these models only work half of the time, but the models could fail because: 1) Δh / $h_{av} \simeq 1$ due to the turbulent layer being thick or close to the ground, 2) there is more than one turbulent layer, or 3) there is a varying angular wind velocity within a single turbulent layer.

4. ATMOSPHERIC NOISE: REMOVAL

In this section we describe various atmospheric noise removal techniques, including one based on the relatively unsophisticated common-mode assumption and several based on the properties of the atmospheric noise determined from our fits to the Kolmogorov-Taylor model. Additionally, we summarize the results of subtracting the atmospheric noise using adaptive principle component analysis (PCA).

4.1 Average Template Subtraction

The most basic method for removing atmospheric noise is to subtract the signal that is common to all of the bolometers. Initially, a template is constructed according to

$$T_n = \frac{\sum_{i=1}^{i=N_b} c_i d_{in}}{\sum_{i=1}^{i=N_b} c_i} \tag{6}$$

where n is the sample number, N_b is the number of bolometers, c_i is the relative responsivity of bolometer i, d_{in} is the signal recorded by bolometer i at sample number n, and T_n is the template. A separate template is computed for each 12.5-second-long scan. After the template is computed, it is correlated with the signal from each bolometer to determine the correlation coefficient, with

$$\tilde{c_i} = \frac{\sum_{j=1}^{j=N_s} T_n d_{in}}{\sum_{j=1}^{j=N_s} T_n^2}. \tag{7}$$

$\tilde{c_i}$ is the correlation coefficient of bolometer i and N_s is the number of samples in the 12.5-second-long scan.[§] Next, the c_i in Equation 6 are set equal to the values of $\tilde{c_i}$ found from Equation 7, and a new template is computed. The process is repeated until the values of c_i stabilize. We generally iterate until the average fractional change in the c_is is less than 1×10^{-8}, which usually takes five to ten iterations. If the c_is fail to converge after 100 iterations, then the scan is discarded from the data. This algorithm generally reduces the RMS of the atmospheric noise by 75%, as shown in Figure 3.

4.2 Wind Model

Since the atmospheric model described in Section 3.2 provided a good description of the atmosphere approximately half of the time, we attempted to improve our atmospheric noise removal algorithm by applying the appropriate time delay/advance to every bolometer prior to average subtraction. Since the fit in Section 3.2 gives the time delay/advance (Δt) as a function of the relative separation and angle between bolometer pairs, it is necessary to pick a reference point on the focal plane. We chose the center as our reference point (i.e., the location where $\Delta t = 0$), and then determined the angle and distance to each bolometer from this point. Next, Δt is determined for each bolometer using the sinusoidal fit for the slope of $2\pi\Delta t/s_{pair}$ versus Θ_{pair}. For example, the plot on the left in Figure 2 has a maximum at a relative bolometer angle of 147 degrees. With our convention for relative bolometer angle, this means the wind is coming from 147 degrees in the bolometer coordinate system. The amplitude of the sin wave is $0.22 = 2\pi\Delta t$, so $\Delta t = 0.035$ seconds for bolometers that are adjacent to each other.

Using the data described above, if a bolometer is located at 4.5 bolometer spacings from the center of the array, at an angle of 127 degrees, then that bolometer will see the atmospheric signal $0.035 \times 4.5 \times \cos(147-127) =$

[§]The best fit correlation coefficients change from one scan to the next, typically by a couple percent.

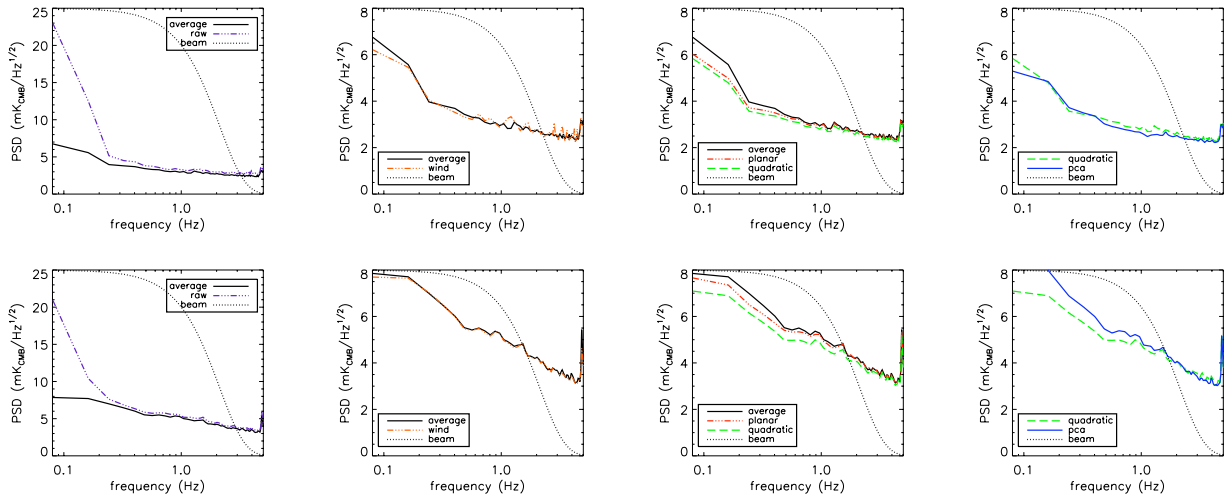

Figure 3. Plots of the time-stream PSDs averaged over all scans and all bolometers for a single observation. The top row shows data from an observation made in relatively good weather, and the bottom row shows an observation made in relatively poor weather. For each plot, the atmospheric subtraction algorithm applied to the data is given in the legend. Overlaid as a dotted line in each plot is the profile of the Bolocam beam.

.175 seconds before a bolometer at the center of the array would. Since our processed data is sampled at 10 Hz, this corresponds to an advance of 1.75 samples. A linear interpolation is used to account for these fractional shifts. Note that this linear interpolation acts as a low-pass filter on our data; to preserve the PSDs of our time-streams we convolve them with a purely real filter of the correct magnitude for each shift. See Appendix A. We applied the appropriate shift to the time-stream of each bolometer before performing average subtraction, but this did not seem to improve the data. See Figure 3. Therefore, we abandoned this atmospheric noise subtraction algorithm.

4.3 Higher-Order Template Subtraction

Based on the Kolmogorov-Taylor model fits, we were able to determine which spatial Fourier modes cause the atmospheric emission to decorrelate over our eight arcminute field of view. Our time-stream PSDs show that most of the atmospheric noise signal is at frequencies below 0.1 Hz, and the atmospheric noise becomes negligible at frequencies above 0.5 Hz. Therefore, most of the atmospheric fluctuations occur on long time-scales, which correspond to large spatial scales. To convert these temporal frequencies to angular frequencies, we divide by the the wind speed we determined for the thin-screen model, which we found in Section 3.2 to be approximately 20 arcminutes/sec. This means that most of the atmospheric noise is at small angular frequencies with $\alpha < 200^{-1}$ arcminutes^{-1}, and the atmospheric noise is negligible for angular frequencies larger than $\alpha = 40^{-1}$ arcminutes^{-1}. We can therefore conclude that very little atmospheric signal is sourced by high angular frequency modes that correspond to wavelengths smaller than our field of view.

Since most of the atmospheric signal is caused by power in angular modes with wavelengths much larger than our field of view, the signal will be slowly varying over our focal plane. This means the variations can be modeled using a low-order two-dimensional polynomial in detector position. Therefore, we decided to try removing a planar fit of atmospheric signal versus bolometer position, and also a two-dimensional quadratic fit of atmospheric signal versus bolometer position. This is similar to the method used by SHARC II to remove atmospheric noise.[16]

For planar and quadratic subtraction, including the special case of average subtraction described in Section 4.1, the algorithm is implemented as follows. The data are modeled according to

$$\vec{d_n} = \mathbf{S}\vec{p_n},$$

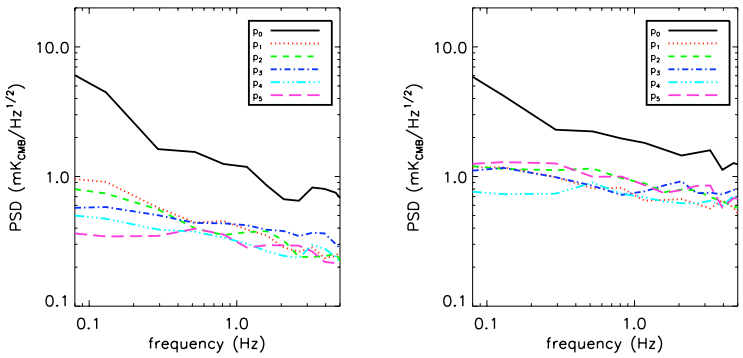

Figure 4. Power spectra for the templates generated by the quadratic sky subtraction algorithm. The plot on the left represents data collected in relatively good weather, and the plot on the right shows data collected in relatively poor weather. All six elements of $\vec{p_i}$ are plotted, with labels given in the upper right of each plot. The higher-order elements in $\vec{p_i}$ are shown for a bolometer approximately half-way between the array center and the edge of the array. Therefore, the PSDs for these $\vec{p_i}$ will be larger for bolometers at the edge of the focal plane, and they will be zero for a bolometer at the center of the focal plane. Note that the magnitude of the higher-order templates in bad weather is a factor of $\simeq 2$ larger than the magnitude of the higher-order templates in good weather.

where $\vec{d_n}$ is a vector with n_b elements representing the bolometer data, $\mathbf{S}$ is an $n_{params} \times n_b$ element matrix, and $\vec{p_n}$ is a vector with n_{params} elements. n_b is the number of bolometers, n is the sample number within the 12.5-second-long scan, and n_{params} is the number of fit parameters. $\mathbf{S}$ is based on the geometry of the focal plane, with $n_{params} = 1/3/6$ for average/planar/quadratic subtraction and

$$\begin{aligned} \text{average: } \mathbf{S} &= (\vec{1}) \\ \text{planar: } \mathbf{S} &= (\vec{1}, \vec{x}, \vec{y}) \\ \text{quadratic: } \mathbf{S} &= (\vec{1}, \vec{x}, \vec{y}, \vec{xy}, \vec{x^2}, \vec{y^2}), \end{aligned}$$

where $\vec{x}/\vec{y}$ are vectors with n_b elements that contain the x/y coordinate of each bolometer. The $\vec{p_n}$ are the n_{params} atmospheric noise templates, which are obtained by minimizing

$$\chi^2_n = (\vec{d_n} - \mathbf{S}\vec{p_n})^T (\vec{d_n} - \mathbf{S}\vec{p_n}) \tag{8}$$

with respect to $\vec{p_n}$.[¶] Each $\vec{p_n}$ can be thought of as a data time-stream that corresponds to a particular spatial dependence over the focal plane. Minimizing Equation 8 yields

$$\vec{p_n} = (\mathbf{S}^T\mathbf{S})^{-1}\mathbf{S}^T\vec{d_n}.$$

Once $\vec{p_n}$ is known, we can construct an atmospheric template analogous to Equation 6 for each bolometer according to

$$\vec{T_n} = \mathbf{S}\vec{p_n}.$$

At this point, the process continues exactly like the average subtraction algorithm given in Section 4.1. A correlation coefficient is computed for each bolometer according to Equation 7, the data is weighted by this correlation coefficient, and a new template is computed. The process is repeated until the fractional change in the values of the correlation coefficients is less than one part in 10^8.

In general, the PSDs of the higher-order templates are $5-10$ times smaller than the PSD of the 0^{th}-order template at low frequency, and 2-5 times smaller than the PSD of the 0^{th}-order template at high frequency for

[¶]The reason there is not a noise covariance matrix in Equation 8 is that we have assumed the instrumental noise is constant in time. Since this noise is approximately white, this should be a reasonable assumption. If the instrumental noise is time-dependent, then our estimate of the atmospheric templates will be noisier, but it will not be biased.

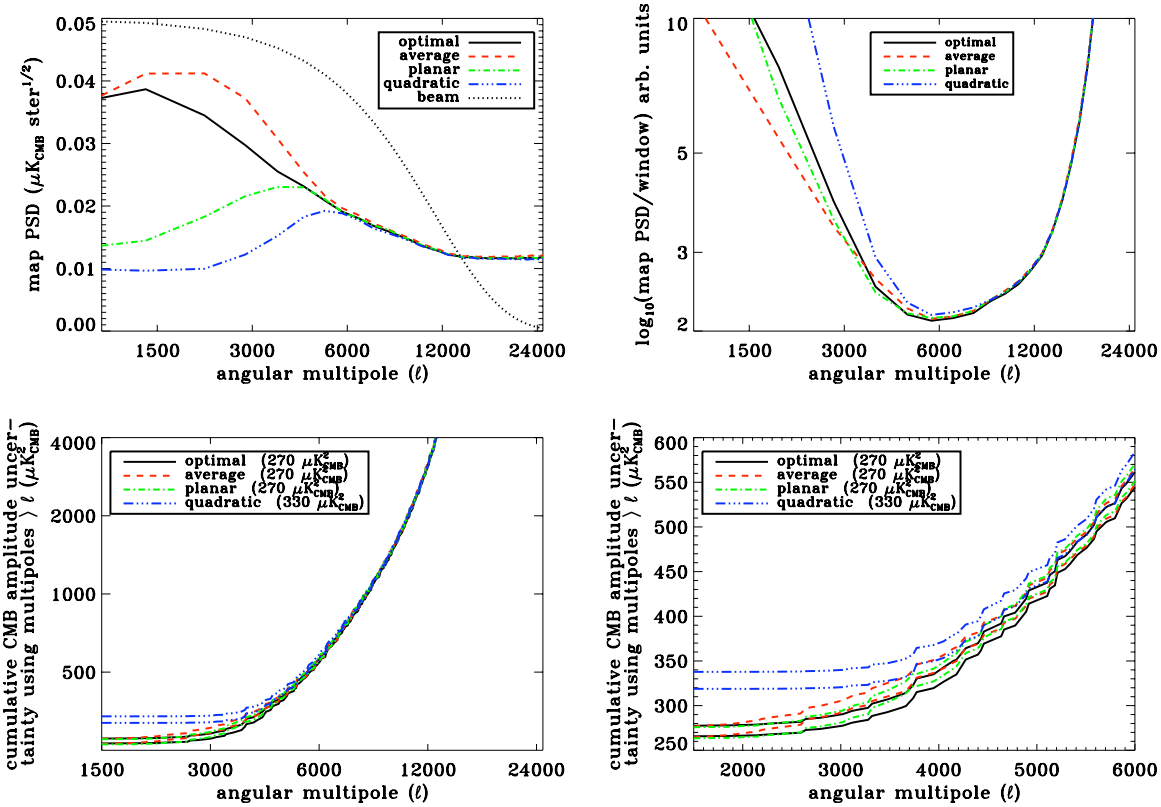

Figure 5. TOP LEFT: The map PSD for all of the Lynx field data, processed using average subtraction, planar subtraction, quadratic subtraction, or the optimal subtraction for each observation. TOP RIGHT: The map PSD for the four data sets divided by the window function for each subtraction algorithm and the window function of the beam. This plot shows the relative sensitivity per unit $\Delta \log(\ell)$ to a flat band power CMB power spectrum in $C_\ell \ell(\ell+1)/2\pi$. Note that average, planar, and optimal subtraction provide the best sensitivity to a CMB power spectrum at some angular scales, but not all angular scales. BOTTOM: Plots of the cumulative sensitivity to a flat band power CMB power spectrum including all of the data at multipoles $> \ell$. The two curves for each data set represent the uncertainty based on the RMS variations in each ℓ-bin. Note that the sensitivity, including all ℓ-bins, is consistent for the average, planar, and optimal data sets. Therefore, our sensitivity to a CMB signal is largely independent of whether average of planar subtraction is used (quadratic is rarely chosen as the optimal method). Additionally, there is little change in the overall sensitivity if the optimal method is chosen by ℓ-bin rather than by observation. This result implies that the CMB signal and the atmospheric noise signal are nearly indistinguishable if they are modeled as linearly varying over our eight arcminute field of view. However, since quadratic subtraction reduces our sensitivity, we can infer that the CMB signal shows more decorrelation on small scales than the atmospheric noise signal, which is reasonable since the power spectrum of the atmosphere goes like $\alpha^{-11/3}$ and the power spectrum of the CMB goes like α^{-2}.

bolometers halfway between the center and the edge of the focal plane. As expected, the ratio of the higher-order templates to the 0^{th}-order template increases as the weather becomes worse. Some examples of the typical power spectra of the $\vec{p_i}$ are shown in Figure 4.

Compared to average sky subtraction, a slight reduction in noise, most noticeable at low frequencies, can be seen in the time-streams. See Figure 3. However, the difference in the noise level of a map made from co-adding all $\simeq 500$ observations of the Lynx science field is significant. See Figure 5. The reason such a small change in the time-stream PSDs produces such a large change in the map PSDs is because planar and quadratic subtraction reduce the amount of correlation between the bolometer time-streams. Figure 6 illustrates this reduction in the correlations by showing the average $xPSD$ for all of our Lynx observations. Note that to isolate the effects of the residual atmospheric noise signal these $xPSD$s were averaged over frequencies below 0.25 Hz.

However, the higher-order templates also remove more astronomical signal compared to average subtraction. Therefore, a single observation of a given astronomical source shape will have an optimal subtraction algorithm based on the noise level of the data and the amount of signal attenuation. For an extended source, (*e.g.*, a flat CMB spectrum in $C_\ell \ell(\ell+1)/2\pi$, where ℓ is angular multipole), we found that average subtraction was optimal for $\simeq 50\%$ of the observations, planar subtraction was optimal for $\simeq 42\%$ of the observations, and quadratic subtraction was optimal for $\simeq 8\%$ of the observations. Although, it should be noted that average and planar subtraction provide very similar sensitivity to a flat CMB power spectrum, likely because the CMB signal is nearly indistinguishable from the atmospheric noise signal for linear variations over our eight arcminute field of view. See Figure 5. For point-like sources we found that average subtraction was optimal for $\simeq 37\%$ of the observations, planar subtraction was optimal for $\simeq 49\%$ of the observations, and quadratic subtraction was optimal for $\simeq 14\%$ of the observations. Most observations were optimally processed with the same algorithm for both point-like and extended objects, indicating that weather is the primary factor in determining which subtraction algorithm will be optimal for a given observation. However, observations of point sources show a slight preference for planar and quadratic subtraction compared to extended sources. This is because the higher-order subtraction algorithms attenuate signal primarily on large scales, so extended objects are more sensitive to the signal loss caused by these algorithms.

4.4 Adaptive Principal Component Analysis (PCA)

We have also used an adaptive PCA algorithm to remove atmospheric noise from Bolocam data.[18,23] The motivation for this algorithm is to produce a set of statistically independent modes, which hopefully convert the widespread spatial correlations into a small number of high variance modes. First, consider the bolometer data to be a matrix, $\mathbf{d}$, with $n_b \times n_s$ elements. As usual, n_b denotes the number of bolometers and n_s denotes the number of samples in a scan. For our adaptive PCA algorithm, we first calculate a covariance matrix, $\mathbf{C}$, with $n_b \times n_b$ elements according to

$$\mathbf{C} = \mathbf{d}\mathbf{d}^T.$$

Next, $\mathbf{C}$ is diagonalized in the standard way to produce a set of eigenvalues (λ_i) and eigenvectors ($\vec{\phi_i}$), where i is the index of the eigenvector and $\vec{\phi}$ contains n_b elements. A transformation matrix, $\mathbf{R}$, is then formed from the eigenvectors according to

$$\mathbf{R} = (\vec{\phi_0}, \vec{\phi_1}, ..., \vec{\phi_{n_b}}).$$

This transformation matrix is used to decompose the data into eigenfunctions, $\vec{\Phi_i}$, with

$$(\vec{\Phi_0}, \vec{\Phi_1}, ..., \vec{\Phi_{n_b}})^T = \mathbf{\Phi} = \mathbf{d}\mathbf{R}^T.$$

At this point, we compute the logarithm for all of the eigenvalues, and then determine the standard deviation of that distribution. All of the eigenvalues with a logarithm more than three standard deviations from the mean are cut, and then a new standard deviation is calculated. The process is repeated until there are no more outliers with large eigenvalues. Next, all of the eigenvector columns, $\vec{\phi_i}$, in $\mathbf{R}$ that correspond to the cut eigenvalues are set to zero, yielding a new transformation matrix, $\mathbf{R}'$. When reconstructing the data, setting these columns in $\mathbf{R}$ equal to zero is equivalent to discarding the cut eigenvectors. Finally, we transform back to the original basis, with the adaptive PCA cleaned data, $\mathbf{d}'$, computed according to

$$\mathbf{d}' = \mathbf{\Phi}\mathbf{R}'.$$

In general, the eigenfunction, $\vec{\Phi_i}$, corresponding to the largest eigenvalue is nearly equal to the template created for average sky subtraction. Therefore, the physical interpretation of the leading order eigenfunction is fairly well understood. However, it is not obvious what signal(s) the lower-order eigenfunctions correspond to.

Typically, adaptive PCA only removes one or two eigenvectors from the data. At high frequencies, adaptive PCA works slightly better than the quadratic method described in Section 4.3, but there is very little astronomical signal at these frequencies because of attenuation by the beam. In good weather, the results from adaptive PCA are comparable to the results from quadratic subtraction, but adaptive PCA performs much worse than quadratic subtraction in bad weather. See Figure 3. However, adaptive PCA attenuates more of the astronomical signal than quadratic subtraction[‖], so adaptive PCA was not used to remove atmospheric noise from the data.

[‖]For a dim point-like source, adaptive PCA removes approximately 19% of the flux, while quadratic subtraction only

5. RESIDUAL TIME-STREAM CORRELATIONS

5.1 Adjacent Bolometer Correlations

In general, for observations made in bad weather, a large number of bolometer pairs have highly correlated time-streams after an atmospheric template is removed from the data. Additionally, the pairs with very large correlations in bad weather are almost always adjacent bolometers. See Figure 6. The reason for the high correlation among adjacent bolometers is the small separation between them on the focal plane, since the horns are only 5 mm, or 0.7 $(f/\#)\lambda$,** on center from each other. Using the optical properties of the telescope and Bolocam optics, along with the geometry of the focal plane, we simulated the amount of correlation between adjacent bolometers for a beam-filling source (like the atmosphere). The result is that approximately 53% of the power received by adjacent bolometers is completely correlated. If the emission from the atmosphere was uniform, then this correlation would be removed by average subtraction since the signal would be correlated among all bolometers, not just adjacent ones. However, since the emission from the atmosphere is not uniform, especially in bad weather, this excess correlation between adjacent bolometer time-streams will not be completely removed by our sky subtraction algorithms. See Figure 6, which shows the average $xPSD$ as a function of the separation between the bolometer pair. The bottom plot in Figure 6 is typical of data collected in poor weather, and shows the large $xPSD$ between adjacent bolometer pairs. A summary of the correlation between the adjacent bolometer pairs for all of the observations is given in Figure 6. Note that the $xPSD$s have been averaged over all frequencies below 0.25 Hz to isolate the effects of the residual low frequency atmospheric noise.

This noise is difficult to remove, because it is only correlated among bolometers that are close to each other on the focal plane. We have attempted to remove this noise by constructing localized templates using the data from a bolometer and the ≤ 6 bolometers that are adjacent to it on the focal plane. We have removed these localized templates from the data both before and after applying our atmospheric noise removal algorithm to the data. Unfortunately, subtracting these templates from the data resulted in an unacceptable amount of signal attenuation, and not all of the locally correlated noise was removed. It should be noted that this excess sub-(f/#)λ correlation has not been appreciated before, and it drives camera design away from sub-(f/#)λ pixel spacing.

5.2 Sensitivity Losses Due to Correlations and Atmospheric Noise

Ideally, the noise in our data would be uncorrelated between bolometers and have a white spectrum. This is approximately what we would expect if instrumental or photon noise was the dominant source of unwanted signal in our data time-streams. However, at low frequencies our data is dominated by atmospheric noise which rises steeply with a $f^{-\delta}$-type spectrum. Additionally, the unremoved atmospheric noise produces correlations between the bolometer time-streams. The atmospheric noise also indirectly creates correlations among the bolometer time-streams due to our removal algorithms. This is because the atmospheric template is a superposition of all the bolometer data, so a small amount of signal from each bolometer is subtracted from the time-stream of every other bolometer when the template is subtracted from the data.

To determine the degradation in our sensitivity to measure a CMB anisotropy caused by these non-idealities in our data, we have created two sets of simulated time-streams. A different simulated data set was generated for each detector for each eight-minute-long observation, based on the measured PSD of each bolometer for each observation. One simulated data set contains randomly generated data with the same noise properties as our actual data, except the simulated data is completely uncorrelated between bolometers. The second set was generated using a flat noise spectrum (i.e., white noise), based on the white noise level observed in our actual data at high frequency. This simulated data set provides a best case scenario for Bolocam. For each simulation we generated data corresponding to all of the observations of the Lynx science field, and the results are shown in Figure 7. Additionally, we made a map from our actual data after masking off 79 of the 115 detectors. This data

removes about 12% of the flux. For reference, average subtraction removes around 2% of the flux and planar subtraction removes approximately 6% of the flux. For a more diffuse source, like the CMB, quadratic subtraction actually attenuates a little more signal than adaptive PCA. However, quadratic subtraction is only used for observations taken in bad weather, and in bad weather quadratic subtraction significantly outperforms adaptive PCA.

**The value of $(f/\#)\lambda$ corresponds to the ratio between the opening diameter of the feed horn and the FWHM of Airy function describing the illumination pattern.

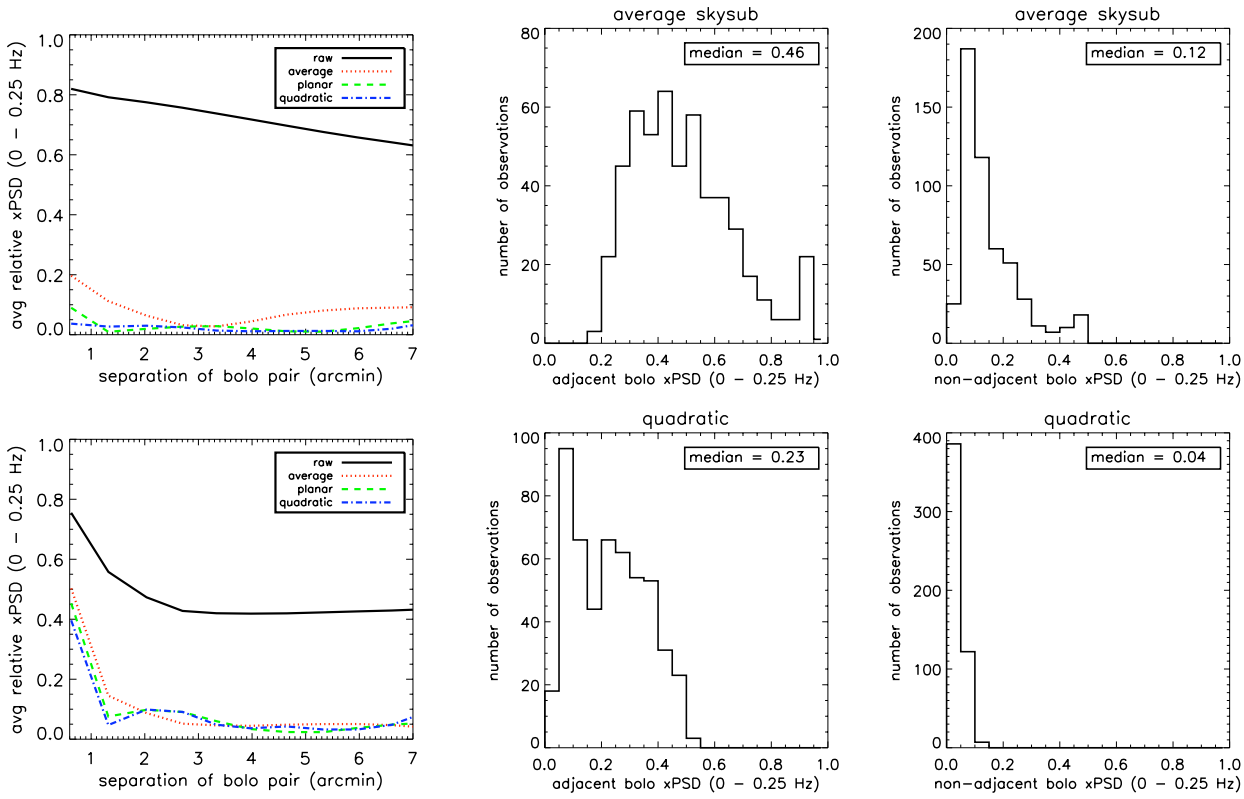

Figure 6. LEFT: Plots of the average xPSD for frequencies below 0.25 Hz for all bolometers for a single observation as a function of bolometer separation. The top plot shows data collected in relatively good weather, and the bottom plot shows data collected in relatively poor weather. Note the residual correlation at small separations that remains after removing an atmospheric template for the data collected in poor weather. For reference, adjacent bolometers are separated by approximately 2/3 arcminute. The reason the correlations in the plots above seem low (*i.e.*, why the raw correlation does not approach 1 as the separation goes to 0) is because of the steep $f^{-\delta}$ profile of the atmospheric noise. The data in the plot above has been averaged over all frequencies below 250 mHz, while most of the power in the time-stream data, which was used to compute the correlations in Figure 1, is at very low frequencies below 100 mHz. CENTER and RIGHT: Histograms of the relative xPSD for frequencies below 0.25 Hz for both adjacent and non-adjacent bolometer pairs. The top row shows data processed with average subtraction, and the bottom row shows data processed with quadratic subtraction. Note the dramatic reduction in correlation for the quadratic-subtracted data compared to the average-subtracted data. Also note the high level of correlation between adjacent bolometer pairs, even with the more aggressive quadratic subtraction method.

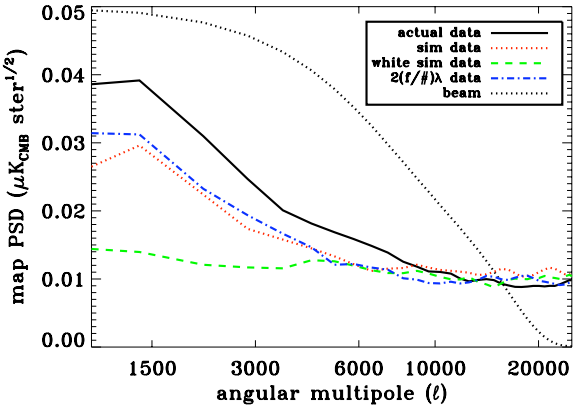

Figure 7. Map PSDs for actual and simulated time-streams. The solid black line shows the map PSD for all of the Lynx data. The red dotted line shows the map PSD for simulated data generated using the noise spectrum of our actual time-streams, except that the simulated data are uncorrelated between detectors. The green dashed line shows the map PSD for uncorrelated simulated data that have a flat frequency spectrum and is based on the white noise level of our actual data. The blue dot-dashed line shows the map PSD for a map made from our actual data, after masking out some detectors so that the spacing between all detectors is at least at least $2(\mathrm{f}/\#)\lambda$. This reduces the number of detectors from 115 to 36, but it discards the highly correlated data between adjacent detector pairs. Note that this spectrum has been multiplied by $\sqrt{36/115}$ to account for the change in the number of detectors. Since this PSD overlaps with the uncorrelated simulated PSD, we can conclude that most of the correlations between detector time-streams are among adjacent detector pairs, and these residual correlations have a significant impact on the noise of the resulting maps.

data type	data spectrum	CMB amplitude uncertainty
actual data	actual data	270 $\mu\mathrm{K}^2_{CMB}$
simulated	actual data	170 $\mu\mathrm{K}^2_{CMB}$
simulated	white	100 $\mu\mathrm{K}^2_{CMB}$
actual data, $2(\mathrm{f}/\#)\lambda$	actual data	170 (550) $\mu\mathrm{K}^2_{CMB}$

Table 1. The estimated uncertainty on measuring the amplitude of a flat CMB power spectrum for all of the Lynx observations. The four data sets include: our actual data, simulated data using our actual time-stream noise spectra, simulated data using our actual time-stream white noise level, and our actual data after masking off 79 of our 115 detectors so that the spacing between all detectors is at least $2(\mathrm{f}/\#)\lambda$. For the two simulated data sets the bolometer time-streams are uncorrelated. The results for the second and fourth data sets are similar, after accounting for the reduction in detector number in the fourth set, indicating that the majority of the correlations between our detector time-streams are between adjacent detector pairs. The results show that our sensitivity to a CMB amplitude is reduced by a factor of $\simeq 1.6$ due to these correlations, and by another factor of $\simeq 1.7$ due to the $f^{-\delta}$-type spectrum of the residual atmospheric noise in our data.

set includes 36 detectors, all of which are separated by more than $2(\mathrm{f}/\#)\lambda$, allowing us to test if the time-stream correlations are isolated to adjacent bolometer pairs. The results from this data set are also shown in Figure 7.

At high spatial frequency ($\ell \gtrsim 10000$) the simulated data sets produce noise levels that are similar to our actual data, which implies that the correlations between detectors occur at low frequency and are caused by the atmospheric noise. However, both simulated data sets have a much lower noise level than our actual data at low spatial frequencies. To quantify the difference between the simulated data sets and our actual data set we have estimated the uncertainty in determining the amplitude of a flat CMB power spectrum. Additionally, we estimated the uncertainty in determining the amplitude of a flat CMB power spectrum for the data set that contains our actual data for 36 detectors. This uncertainty was multiplied by 36/115 to account for the degradation caused by masking off 79 detectors. The results are shown in Table 1. The simulated data indicate that our uncertainty on the amplitude of a flat CMB power spectrum would be improved by a factor of $\simeq 1.6$ if the detector time-streams were uncorrelated, and by another factor of $\simeq 1.7$ if the time-streams had a white

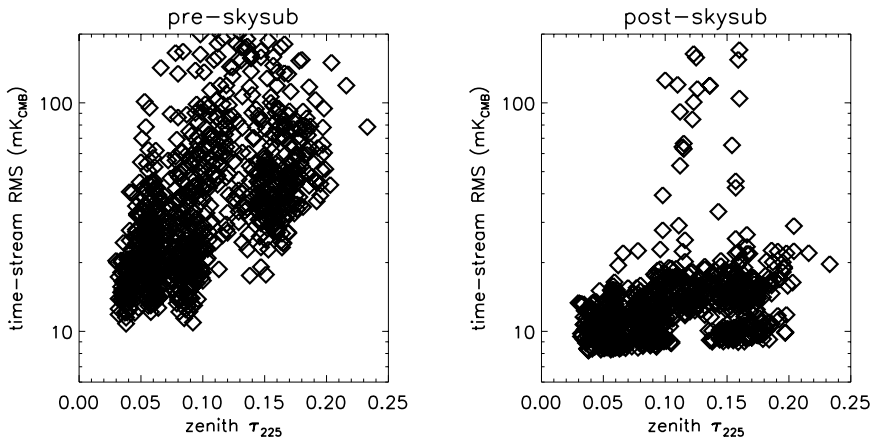

Figure 8. Plots of the time-stream RMS as a function of zenith atmospheric opacity at 225 GHz. The plot on the left shows data prior to removing atmospheric noise, and the plot on the right shows data after subtraction of an average template. Note that there is little or no correlation between the amount of atmospheric noise as measured by the time-stream RMS and the amount of water vapor as measured by the atmospheric opacity.

spectrum instead of the $f^{-\delta}$-type spectrum due to the residual atmospheric noise.

Additionally, after correcting for the loss of 79 detectors, the data set with 36 detectors produces a similar result to the simulated data set based on our actual noise spectra. This indicates that the correlations between time-streams of non-adjacent bolometers are negligible. The implication is that if we had used larger horns (in $(\mathrm{f}/\#)\lambda$) while maintaining the same number of detectors we would have improved our sensitivity by a factor of 1.6. By going to larger horns we would also have a larger field of view, which would have both positive (*e.g.*, sensitivity to larger scales) and negative (*e.g.*, less uniform map coverage) effects on our data. A larger field of view may also require higher-order polynomial subtraction, since the focal plane would be closer in size to the angular scale of the dominant atmospheric noise modes. However, it seems likely that these effects would be small compared to the large gain in sensitivity we would achieve by eliminating the correlations between bolometer time-streams. Another implication is that increasing the number of detectors by a factor of N for a fixed field of view will not produce the factor of N increase in mapping speed that would be achieved by expanding the field of view proportionally to the number of detectors. As mentioned earlier, this fact had not been previously appreciated, and will drive ground-based camera design away from sub-$(\mathrm{f}/\#)\lambda$ pixel spacings. Therefore, a larger field of view will be required to increase the number of pixels for a given instrument, and such cameras may need to rely on higher-order polynomials to remove the atmospheric noise.

6. ATMOSPHERIC NOISE AS A FUNCTION OF ATMOSPHERIC OPACITY

Ironically, we found almost no correlation between the amount of water vapor in the atmosphere and the magnitude of the atmospheric noise in our data. We compared the value of the atmospheric opacity measured by the CSO τ-meter, which corresponds to the amount of water vapor in the atmosphere, to the RMS of our time-stream data, which is a good proxy for the amount of atmospheric noise in our data. The results are shown in Figure 8, and show no evidence of correlation. For raw data the Pearson's correlation coefficient between τ_{225} and time-stream RMS is $r = 0.21$, and for average subtracted data $r = 0.16$. Note that Bussmann et al.[2] find a similar lack of correlation between opacity and sensitivity for ACBAR data collected at the South Pole. It is not clear why there is little or no correlation between the amount of water vapor in the atmosphere and the amount of atmospheric noise in our data. However, a possible explanation is that the clumpiness of the water vapor in the atmosphere is largely independent of the total amount of water vapor in the atmosphere.

7. CONCLUSIONS

We have studied the atmospheric noise above Mauna Kea with Bolocam at 143 GHz using data collected in late 2003 and spanning approximately 40 nights. The data are dominated by $f^{-\delta}$ atmospheric noise at frequencies

$\lesssim 0.5$ Hz in all observing conditions. In approximately half our data we were able to model the fluctuations in atmospheric emission using a Kolmogorov-Taylor turbulence model for a thin wind-driven screen of water vapor. Based on the results of this modeling, we concluded that a low-order polynomial in detector position over the 8 arcminute focal plane is the optimal way to describe the fluctuations in atmospheric emission. However, after modeling and removing the atmospheric noise using these algorithms, the data is still dominated by atmospheric noise at frequencies below $\simeq 0.5$ Hz in all of the data. Therefore, spatial subtraction of atmospheric noise on scales of several arcminutes will not allow BLIP performance below $\simeq 0.5$ Hz for broadband 143 GHz receivers operating at the CSO.

However, this does not mean that BLIP performance is impossible from the CSO. SUZIE I.5 was able to achieve instrument limited performance[††] down to 10 mHz at 150 GHz at the CSO by subtracting a combination of spatial and spectral common mode signals.[22] The initial subtraction of the spatial common mode signal is obtained from differencing detectors separated by $\simeq 4$ arcminutes, and removes the atmospheric noise to within a factor of two of the instrument noise level below a couple hundred mHz. However, SUZIE I.5 had three observing bands (1.1, 1.4, and 2.1 mm) per spatial pixel, which allowed determination of the correlated signal over a range of frequencies. The remaining atmospheric noise at low frequency can be removed down to the instrument noise level by subtracting this spectral common mode signal.

SUZIE II was able to employ a similar subtraction method, using observing bands at 0.85, 1.4, and 2.1 mm for each spatial pixel.[1] Additionally, SUZIE II has a much lower instrument noise level at 150 GHz compared to SUZIE I.5, within 50% of the BLIP limit. Similar to Bolocam, SUZIE II reaches the instrument noise level at frequencies above a couple hundred mHz by subtracting a spatial common mode signal. However, by subtracting the spectral common mode signal SUZIE II achieves instrument noise limited performance below 100 mHz, and is within a factor of 1.5 of the instrument noise limit at 10 mHz. Therefore, spectral subtraction of the atmospheric noise does provide a method to achieve BLIP, or nearly BLIP, performance from the CSO.

APPENDIX A.

In order to account for the time lags and advances between bolometer time-streams that are described by the Kolmogorov-Taylor thin-screen model we in general have to shift the time-streams by a fractional number of samples. For example, if a given bolometer time-stream is advanced by Δt_b seconds, then we will account for this advance by shifting the time-stream according to

$$d'_n = \left(1 - \left|\frac{\Delta t_b}{\Delta t}\right|\right) d_n + \left|\frac{\Delta t_b}{\Delta t}\right| d_{n+\Delta t_b/\Delta t} \tag{9}$$

where d'_n is the interpolated data time-stream, d_n is the original data time-stream, Δt is the time between samples, and n is the sample number. Note that we have assumed that $\Delta t_b < \Delta t$, since shifts by integer multiples of Δt are trivial. Alternatively, this shift can be performed in frequency space by applying

$$S_m = \left(1 - \left|\frac{\Delta t_b}{\Delta t}\right| + \left|\frac{\Delta t_b}{\Delta t}\right| e^{-\mathrm{sign}(\Delta t_b) i 2\pi f_m \Delta t}\right)$$

to the Fourier transform of the time-stream data, where f_m is frequency in Hz and m is the frequency-space index. S_m acts like a filter, and for all non-zero frequencies $|S_m| < 1$. Therefore, to preserve the noise properties of our data, we divide the Fourier transform of the shifted time-stream by $|S_m|$. In summary, we shift the time-stream data according to Equation 9, then correct for the filtering effects of this shift in frequency-space by dividing by $|S_m|$.

REFERENCES

[1] Benson, B. A., "Spectral Measurements of the Sunyaev-Zel'dovich Effect", PhD Thesis, Stanford (2004).

[††]For reference, SUZIE I.5's BLIP limit is a factor of $\simeq 3$ below the instrument noise limit at 100 mHz and a factor of $\simeq 6$ below the instrument noise limit at 10 mHz.

[2] Bussmann, R. S., Holzapfel, W. L., and Kuo, C. L., "Millimeter Wavelength Brightness Fluctuations of the Atmosphere above the South Pole", ApJ, 622, 1343-1355 (2005).
[3] Chamberlin, R. A., "Notes on Tau sky monitors" http://www.cso.caltech.edu/taumeter.txt (1999).
[4] Church, S. E., "Predicting residual levels of atmospheric sky noise in ground based observations of the cosmic microwave background radiation", MNRAS, 272, 551-569 (1995).
[5] Dobbs, M. et al., "APEX-SZ first light and instrument status", New Astr. Rev., 50, 960-968 (2006).
[6] Dowell, C. D. et al., "SHARC II: a Caltech submillimeter observatory facility camera with 384 pixels", Proc. SPIE, 4855, 73-87 (2003).
[7] Glenn, J. et al., "Bolocam: a millimeter-wave bolometric camera", Proc. SPIE, 3357, 326-334 (1998).
[8] Glenn, J. et al., "Current status of Bolocam: a large-format millimeter-wave bolometer camera", Proc. SPIE, 4855, 30-40 (2003).
[9] Golwala et al., in preparation (2008).
[10] Haig, D. J. et al., "Bolocam: status and observations", Proc. SPIE, 5498, 78-94 (2004).
[11] Holland, W. S. et al., "SCUBA: a common-user submillimetre camera operating on the James Clerk Maxwell Telescope", MNRAS, 303, 659-672 (1999).
[12] Kreysa, E. et al., "Bolometer array development at the Max-Planck-Institut fuer Radioastronomie", Proc. SPIE, 3357, 319-325 (1998).
[13] Kreysa, E. et al., "LABOCA: a first generation bolometer camera for APEX", Proc. SPIE, 4855, 41-48 (2003).
[14] Kolmogorov, A. N., "The Local Structure of Turbulence in an Incompressible Fluid with Very Large Reynolds Number", ANSSSR, 30, 301-305 (1941).
[15] Kosowsky, A., "The Atacama Cosmology Telescope", New Astr. Rev., 47, 939-943 (2003).
[16] Kovacs, A., "SHARC-2 350 micron observations of distant submillimeter-selected galaxies and techniques for the optimal analysis and observing of weak signals", PhD Thesis, Caltech (2006).
[17] Lane, A. P., "Submillimeter Transmission at South Pole", Astro. Antarctica, 141, 289 (1998).
[18] Laurent, G. T. et al., "The Bolocam Lockman Hole Millimeter-Wave Galaxy Survey: Galaxy Candidates and Number Counts", ApJ, 623, 742-762 (2005).
[19] Lay, O. P. and Halverson, N. W., "The Impact of Atmospheric Fluctuations on Degree-Scale Imaging of the Cosmic Microwave Background", ApJ, 543, 787-798 (2000).
[20] Masson, C. R., "Atmospheric Effects and Calibrations", IAU Colloq. 140, 59, 87 (1994).
[21] Mauskopf, P. D., Bock, J. J., Del Castillo, H., Holzapfel, W. L., and Lange, A. E., "Composite infrared bolometers with Si 3 N 4 micromesh absorbers", Appl. Optics, 36, 765-771 (1997).
[22] Mauskopf, P. D., "Measurements of Anisotropies in the Cosmic Microwave Background at Small and Intermediate angular scales with Bolometric Receivers at mm Wavelenghts", PhD Thesis, University of California at Berkeley (1997).
[23] Murtagh, F. and Heck, A., [Multivariate Data Analysis], Kluwer Academic Publishers, Boston (1987)
[24] Pardo, J. R., Cernicharo, J., and Serabyn, E., "Atmospheric transmission at microwaves (ATM): an improved model for millimeter/submillimeter applications", IEEE Trans. Ant. Prop., 49, 1683-1694 (2001).
[25] Peterson, J. B., Radford, S. J. E., Ade, P. A. R., Chamberlin, R. A., O'Kelly, M. J., Peterson, K. M., and Schartman, E., "Stability of the Submillimeter Brightness of the Atmosphere above Mauna Kea", Publ. Astron. Soc. Pac., 115, 383-388 (2003).
[26] Radford, S. J. and Chamberlin, R. A., ALMA memo 334 (2000).
[27] Ruhl, J. et al., "The South Pole Telescope", Proc. SPIE, 5498, 11-29 (2004).
[28] Sayers, J. et al., "A search for cosmic microwave background anisotropies on arcminute scales with Bolocam", preprint (astro-ph/08053151).
[29] Stark, A. A., et al., "The Antarctic Submillimeter Telescope and Remote Observatory (AST/RO)", Publ. Astron. Soc. Pac., 113, 567-585 (2001).
[30] Tatarskii, V. I., [Wave Propagation in a Turbulent Medium], McGraw-Hill, New York (1961).
[31] Taylor, G. I., "The Spectrum of Turbulence", Proc. R. Soc. Lond. A, 164, 476-490 (1938).
[32] Wright, M. C. H., "Atmospheric Phase Noise and Aperture Synthesis Imaging at Millimeter Wavelengths", Publ. Astron. Soc. Pac., 108, 520-534 (1996).